Title

Polarization-Insensitive Holographic Surfaces With Broadside Radiation

Journal

IEEE Transactions on Antennas and Propagation, 64(12)

ISSN

0018-926X

Authors

Li, Mei
Xiao, Shao-Qiu
Sievenpiper, Daniel F

Publication Date

2016-12-01

DOI

10.1109/tap.2016.2618853

Peer reviewed

Polarization-Insensitive Holographic Surfaces With Broadside Radiation

Mei Li, *Student Member, IEEE*, Shao-Qiu Xiao, *Member, IEEE*, and Daniel F. Sievenpiper, *Fellow, IEEE*

***Abstract*— Scalar holographic surfaces (HSs) with a unique polarization-insensitive property are presented. The proposed HSs are constructed by sinusoidally modulated loop-wire unit cells, which can support both TE mode and TM mode propagation with the same phase velocity. The modulation principle in terms of refractive index is presented, which is convenient for HS designs concerning both TE and TM modes. A scalar polarization-sensitive HS using square patches exhibits a mismatch in the E- and H-plane beamwidths due to the sin (φ) circumferential illumination of the x-directed dipole, resulting in a low aperture efficiency. Two novel scalar HS designs using loop-wire configuration in square lattice and hexagonal lattice are proposed which exhibit the polarization-insensitive property with nearly circularly symmetric E- and H-plane beamwidths when illuminated by an x-directed dipole. Both simulations and measurements are carried out in this paper, which agree well with each other.**

***Index Terms*— Holographic surfaces (HSs), leaky-wave antennas, metasurfaces, modulated surfaces.**

I. Introduction

A HOLOGRAPHIC surface (HS) is a kind of modulated artificial surface based on the interference pattern between the currents generated by a source, which can be a small feed or a plane wave impinging on the surface, and the desired fields, which can be radiating leaky waves or bound surface waves [1]. HSs are usually constituted by a series of modulated conducting strips [2]–[6] or subwavelength, electrically small periodic unit cells [1]. By properly engineering the geometrical dimensions of the unit cells, the effective surface impedance can be modulated. Due to the simple manufacture process using standard printed-circuit techniques, HSs have the advantages of low cost, low profile, lightweight, and conformability, and thus have gained increasing attention in recent years.

One predominant application of HSs is holographic antennas and also known as impedance modulated surfaces, which are essentially leaky-wave antennas with radiation performance of high gain and pencil beams. In 1959, Oliner and Hessel [7] studied the propagation characteristics and field distributions of waves guided by a sinusoidally modulated reactance surface. A printed, 1-D leaky-wave antenna with a sinusoidally modulated surface reactance was designed in [5]. 2-D holographic antennas using scalar and tensor holographic artificial impedance surfaces were proposed in [1], demonstrating that a tensor impedance surface can provide control over polarization. Minatti *et al.* [8], [10], Faenzi *et al.* [9], and Pereda *et al.* [11] have done intensive study on circularly polarized holographic antennas including using scalar impedance surfaces with a spiral modulation as well as tensor impedance surfaces to properly polarize the aperture field. In [11], two synchronized modes (TE and TM modes) with the same phase velocity are generated by selecting an appropriate tensor modulated surface and an LHCP or RHCP antenna is then obtained when the circular waveguide-feed is excited with two mutually orthogonal TE_{11} modes in phase-quadrature. It is reported in [12] that by varying the relative phase of the sinusoidal modulation of the different regions of a scalar impedance HS, it is possible to obtain a desired pencil beam with a desired polarization. Besides the application of holographic antennas, HSs can also be applied to the field of surface-wave manipulation. A focusing HS, which can convert the incoming propagating waves to surface waves and then focus on a spot, is presented in [13]. This mechanism can be seen as the inverse process of a holographic antenna. HSs have also been reported to be used in the aspect of near-field focusing [14] and radar cross section reduction [15].

Scalar impedance surfaces generally support the propagation of either a TM or a TE lower order surface-wave mode at a given frequency. For a vertically polarized (TM) surface-wave excitation, for instance, a circularly symmetric E- and H-plane beamwidth can be achieved when the HS, as shown in Fig. 1, is constituted by a scalar artificial surface supporting TM surface waves (namely, TM-type HS) [10]. However, for a horizontally polarized incidence wave originating from an x- or y-directed infinitesimal electric dipole, the radiation pattern of one plane (E- or H-plane) exhibits noticeably wider beamwidth than that of the other plane (H- or E-plane), regardless of whether

Manuscript received July 27, 2016; revised September 9, 2016; accepted September 14, 2016. Date of publication October 19, 2016; date of current version December 5, 2016. This work was supported in part by AFOSR under Grant FA9550-16-1-0093, in part by the China Scholarship Council, and in part by the National High Technology Research and Development Program under Grant 2015AA7124075A.

M. Li is with the College of Communication Engineering, Chongqing University, Chongqing 400044, China, and also with the Department of Electrical and Computer Engineering, University of California at San Diego, La Jolla, CA 92093 USA (e-mail: li.mei@cqu.edu.cn).

S.-Q. Xiao is with the School of Physical Electronics, University of Electronic Science and Technology, Chengdu 610054, China (e-mail: xiaoshaoqiu@uestc.edu.cn).

D. Sievenpiper is with the Electrical and Computer Engineering Department, University of California at San Diego, La Jolla, CA 92130 USA (e-mail: dsievenpiper@eng.ucsd.edu).

Color versions of one or more of the figures in this paper are available online at http://ieeexplore.ieee.org.

Digital Object Identifier 10.1109/TAP.2016.2618853

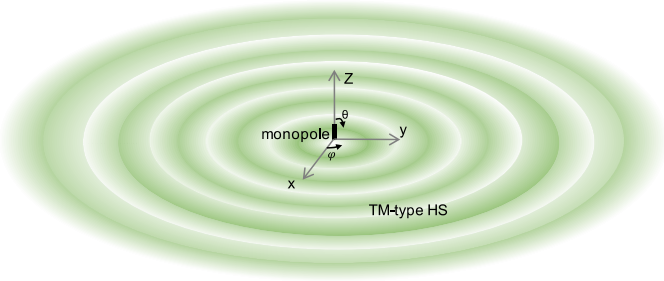

Fig. 1. TM-type HS with z-directed monopole excitation.

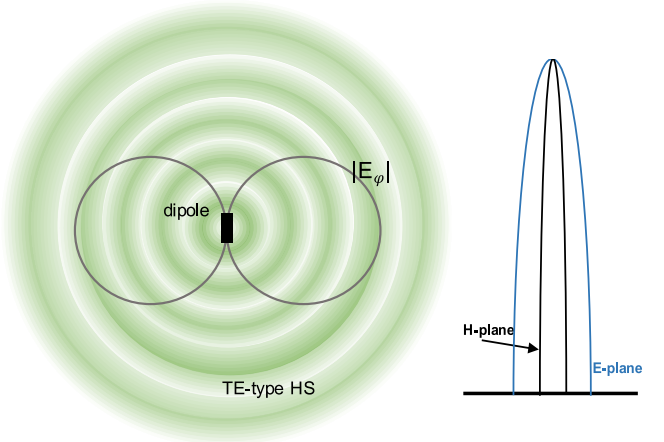

(a) (b)

Fig. 2. TE-type HS with horizontal dipole excitation. (a) Sin(φ) circumferential illumination of the HS by the x-directed electric dipole. (b) E- and H-plane radiation patterns with different beamwidths.

the HS is composed of a TM- or TE-type scalar impedance surface [3], [16]. Fig. 2 shows a sinusoidally modulated HS composing of a TE-type scalar metasurface excited by a small, x-directed electric dipole. The HS is thereby sin(φ) circumferentially illuminated by the dipole. As a result, the radiation pattern in the E-plane is much wider than that of H-plane [as shown in Fig. 2(b)], which would result in a low aperture efficiency. This part of work will be illustrated in detail in Section III. With the aid of tensor impedance surfaces, it is possible to obtain a rotationally symmetric pencil beam from a horizontal, linearly polarized excitation [11]. Instead of using tensor HSs, this paper focuses on utilizing scalar metasurfaces to realize this radiation property aiming to improve the aperture efficiency. The unit cell structure of the scalar metasurfaces is based on the polarization-insensitive, double-layered, and loop-wire configuration proposed in [17], which can support both TM and TE modes with the same phase velocity.

This paper is organized as follows. Section II presents the modulation principle of the HSs in terms of refractive index. Based on this modulation principle, a polarization-sensitive HS consisting of metallic square patches is proposed and analyzed when excited by an x-directed small electric dipole in Section III. Polarization-insensitive HS using loop-wire unit cells arranged in square lattice and hexagon lattice are proposed in Sections IV and V, respectively. The characteristics of these two HSs are investigated both by simulation and measurement. Then, conclusions are drawn in Section VI.

II. Modulation Principle of Holographic Surfaces

Instead of modulating the surface impedance to synthesize an HS, as is widely used in [1], here, the propagation constant is sinusoidally modulated by the following expression:

$$\beta = \beta_0 + m\cos\left(\frac{2\pi}{a}\rho\right) \tag{1}$$

where β_0 is average propagation constant and also represents the unperturbed value of β with $m = 0$, m is the modulation factor, a is the period of the modulation, and ρ is the radial distance from the center point in a cylindrical coordinate system.

Because of the one-to-one mapping of propagation constant values with modulated geometry, the HSs obtained by sinusoidally modulated propagation constant correspond to a sinusoidally modulated periodic surface. Based on Floquet theory, the propagation constant of a periodic structure can be written as follows:

$$\beta_{tp} = \beta_{t0} + \frac{2\pi p}{a} = \beta_0 + \Delta\beta + \frac{2\pi p}{a} \tag{2}$$

where p $(0, \pm 1, \pm 2\ldots)$ is the index of the Floquet mode, β_{t0} is the propagation constant of the Floquet mode with an index of $p = 0$, and $\Delta\beta$ is perturbation of β caused by the non-zero modulation m. β_{t0} is close to β_0 when the modulation of the surface is small [5]. Therefore

$$\beta_{tp} \approx \beta_0 + \frac{2\pi p}{a}. \tag{3}$$

The beam direction θ_0 can be determined from

$$\sin(\theta_0) = \frac{\beta_{t(-1)}}{k_0} = \frac{\beta_0 - \frac{2\pi}{a}}{k_0}. \tag{4}$$

Considering the case of normal radiation (equally, plane waves normally illuminating the surface), there is $\theta_0 = 0°$. Therefore, it can be obtained that $a = (2\pi/\beta_0)$, and (1) can be rewritten as

$$\beta = \beta_0 + m\cos(\beta_0\rho). \tag{5}$$

Dividing k_0, i.e., the wavenumber in the free space, to both sides of the equation, we have

$$\frac{\beta}{k_0} = \frac{\beta_0}{k_0} + \left(\frac{m}{k_0}\right)\cos(\beta_0\rho). \tag{6}$$

Let $n = \beta/k_0$, $X = \beta_0/k_0$, and $M = m/k_0$. Then

$$n = X + M\cos(Xk_0\rho) \tag{7}$$

where n represents effective refractive index, X represents the average refractive index and determines the period of the modulation, and M is the modulation depth. X and M can be properly chosen in each individual HS design. Note that $X > 1$ in (7) should be met such that no other spatial harmonics radiate besides the $p = -1$ harmonic. Meanwhile, M should be small enough to be consistent with (3).

Equation (7) provides the modulation principle in terms of effective refractive index to synthesize an HS and will

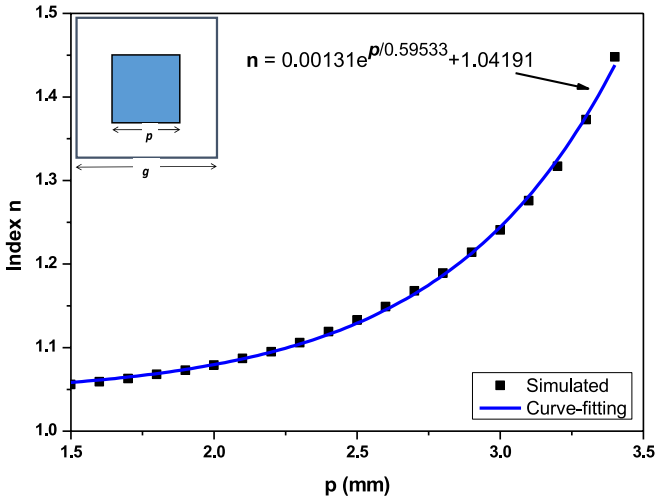

Fig. 3. Effective refractive index as a function of length p at 15 GHz. Scatters show the result of HFSS calculations, and the line is obtained by curve-fitting. The lattice constant of the unit cell is $g = 3.5$ mm.

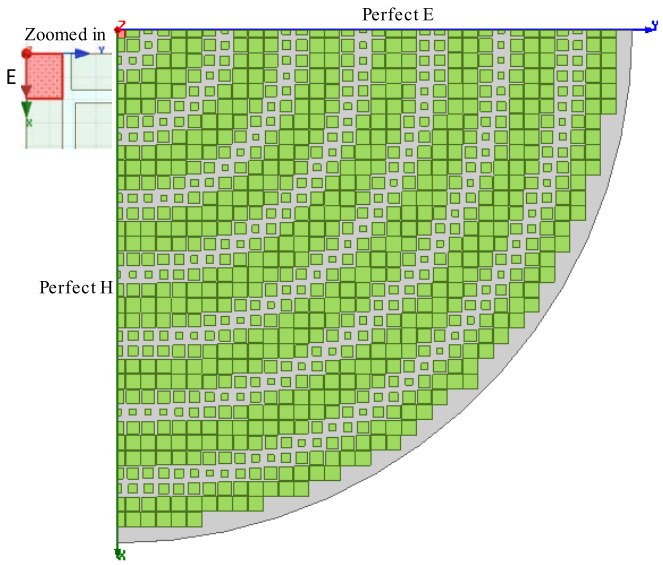

Fig. 4. Quarter of the HS in circular layout with a radius of $R = 5.87\lambda_0$, where λ_0 corresponds to the free-space wavelength at a frequency of 15 GHz. Symmetric boundaries (i.e., perfect E and perfect H) are used to simplify the simulation. A lumped port with the electric field E aligned with the x-axis (shown in the red shadow) is assigned at the center. X and M in (7) take the value 1.252 and 0.196, respectively.

be employed to synthesize all of the HS proposed in this paper. Using index instead of surface impedance to express the modulation formula offers the following convenience: On the one hand, the conventional calculation process from index to surface impedance and then to modulated geometry is simplified. Here, index is directly mapped to the modulated geometry. The need for intermediate surface impedance calculation is avoided. One the other hand, regardless of TE or TM mode, X and M in (7) stay the same so as to guarantee the phase matching of these two kinds of modes, i.e., $X_{\mathrm{TE}} = X_{\mathrm{TM}}$ and $M_{\mathrm{TE}} = M_{\mathrm{TM}}$, as demonstrated in Sections IV and V. In contrast, when the modulation principle is expressed in terms of surface impedance, the average impedance X [1] of TE and TM modes is different and so is the corresponding modulation depth M [1].

III. Polarization-Sensitive Holographic Surface Design Using Square Patches

In this section, an HS constructed by subwavelength conductive square patches is designed by using (7). Those square patches are printed on the top layer of a bare dielectric with a relative permittivity of 2.2 and thickness of 1.575 mm. It is known that arrays constructed by discrete patches without a ground plane predominantly support TE-type surface waves. Fig. 3 plots the simulated effective refractive index n as a function of the patch length $p$at a frequency of 15 GHz for a periodically infinite array. The geometry of the unit cell and nonlinear curve fit are also provided in Fig. 3. ANSYS HFSS was used for simulation in this paper.

An HS in circular layout with a radius of R is proposed in this paper. As shown in Fig. 4, a quarter of the HS with symmetric boundaries is modeled to simplify the simulation. The HS is generated using (7) with the values of $X = 1.252$ and $M = 0.196$. In order to investigate the performance of the proposed surface, a lumped port with E-field aligned with the x-axis is assigned at the center to excite the surface.

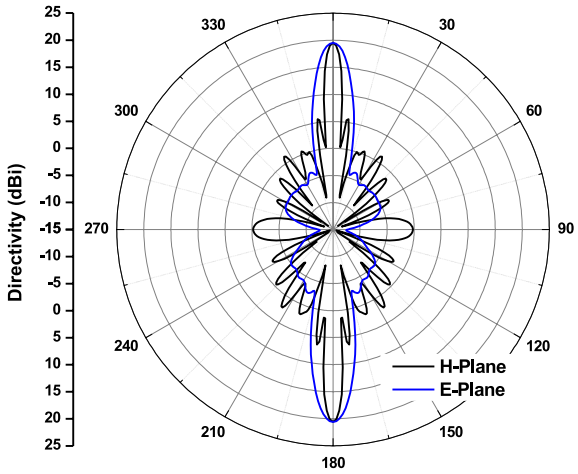

Fig. 5. Radiation patterns of the HS constituted by conductive patches. The directivity is 20.6 dBi at $\theta = 180°$ direction and 19.5 dBi at $\theta = 0°$ direction. The slight difference in directivity is due to the presence of dielectric. The return loss due to impedance mismatch is not included in the radiation patterns.

Radiation patterns and field distributions are analyzed to examine the surface performance. Fig. 5 shows the radiation patterns of the HS. As can be seen from Fig. 5, the patterns in the H- and E-plane differ greatly in beamwidth. A narrow beam is shaped in the H-plane, while a much broader beam is formed in the E-plane, which is consistent with the analysis in Fig. 2. As a result, the aperture efficiency $((D\lambda^2)/(4\pi A)$, where D is the directivity and A is the physical size of the HS) of the HS is 8.72% when considering the backward beam ($\theta = 180°$) only and 15.27% when considering both the forward ($\theta = 0°$) and backward beams.

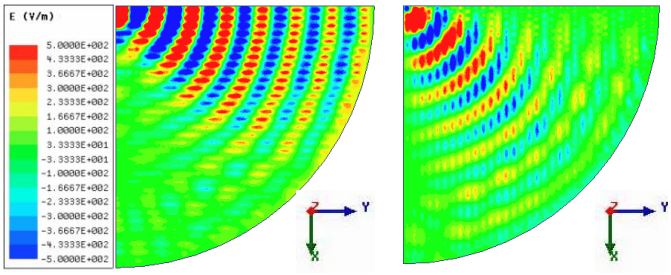

Fig. 6. Field distributions of (a) E_x component and (b) E_y component on a reference plane with a distance of 1 mm above the HS.

The field distributions of the E_x and E_y components along the HS are investigated to get a better understanding of the radiation mechanism. Assume the electric field of the excitation has the form of $E_0\vec{x}$. In the cylindrical coordinates system, there is

$$\vec{e_x} = \vec{e_\rho}\cos(\varphi) - \vec{e_\varphi}\sin(\varphi). \tag{8}$$

For a TE-type HS, only E_φ component can propagate along the HS. Therefore, the fields on the HS are as follows:

$$E_\varphi = -E_0\sin(\varphi) \text{ (as the plot shown in Fig. 2)} \tag{9a}$$

$$E_\rho = 0. \tag{9b}$$

Since

$$\vec{e_\varphi} = -\vec{e_x}\sin(\varphi) + \vec{e_y}\cos(\varphi). \tag{10}$$

Therefore, according to (9a), (9b), and (10), E_x and E_y components on the HS have the following forms:

$$E_x = -E_\varphi\sin(\varphi) = E_0\sin^2(\varphi) = \frac{E_0}{2}(1-\cos(2\varphi)) \tag{11}$$

$$E_y = E_\varphi\cos(\varphi) = -\frac{E_0}{2}\sin(2\varphi). \tag{12}$$

The field distributions of the E_x and E_y components on a reference plane with a distance of 1 mm above the HS are shown in Fig. 6. As can be seen from Fig. 6(a), E_x component is concentrated around the y-axis ($\varphi = 90°$) and is nearly zero along the x-axis ($\varphi = 0°$), which is consistent with (11). According to Fig. 6(b), the E_y component has the maximum at the $\varphi = 45°$ direction and the minimum at the $\varphi = 0°$ and $\varphi = 90°$ directions, which perfectly agree with (12).

To sum up, an x-directed dipole on a TE-type HS would result in a much wider beamwidth in the E-plane than that in the H-plane. Similarly, an x-directed dipole on a TM-type HS would result in a wider beamwidth in the H-plane compared to that in the E-plane. Therefore, it can be concluded that HSs supporting only the TM or TE mode would result in a low aperture efficiency in the cases of horizontal dipole excitation due to their polarization-sensitive property. In order to overcome this disadvantage, polarization-insensitive metasurfaces that simultaneously support both TM and TE modes are utilized to achieve a pencil beam with nearly circularly symmetric E- and H-plane beamwidths in the following sections. Other methods to improve the aperture efficiency include using tapered modulation, as reported in [18].

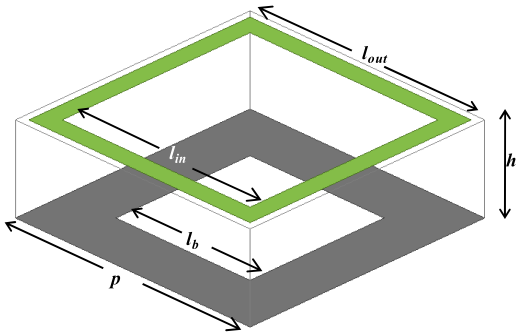

Fig. 7. Loop-wire unit cell in square lattice.

IV. Polarization-Insensitive Holographic Surface Design Using Loop-Wire Cells in Square Lattice

A. Unit Cell Design

In general, scalar metasurfaces dominantly support either the TM or TE mode at a given frequency, and limitations exist due to such polarization sensitivities. It is reported in [17] that surface waveguides composed of two frequency-selective surfaces (FSSs) layers whose dominant modes are TE and TM, respectively, can be designed to exhibit the property of supporting both TE and TM modes with the same phase velocity at a given frequency. Specifically, a square loop-wire configuration, as shown in Fig. 7, can achieve such polarization-insensitive property. A conductive square loop and a conductive wire-grid are printed at the top and bottom layer of a dielectric with a thickness of $h = 1.575$ mm and relative permittivity of $\varepsilon_r = 2.2$. The square lattice constant of the unit cell is $p = 3.5$ mm. The outer edge length of the square ring is kept as a constant of $l_{\text{out}} = 3.3$ mm. The lengths of the inner edges of the square loop and the wire-grid are l_{in} and l_b, respectively.

The square loop-wire unit cells with the same dimensions as shown in Fig. 7 are utilized to synthesize the polarization-insensitive HS. In order to enable the phase matching of TE and TM modes, it is necessary to guarantee that propagation constants of TE and TM modes are the same. The modulation principle of such an HS becomes

$$n_{\text{TE}} = n_{\text{TM}} = X + M\cos(Xk_0\rho). \tag{13}$$

The next step is to determine the effective refractive index as a function of the geometric parameters of the unit cell. Note that, compared to a purely TE- or TM-type HS as that in Section III, one additional requirement needs to be met: the dispersion curves of the TE and TM modes must overlap at the HS operation frequency, satisfying $n_{\text{TE}} = n_{\text{TM}}$. By properly choosing the values of l_{in} and l_b, the refractive index of TE and TM modes can be tuned simultaneously, as shown in Fig. 8. For illustration, Fig. 8 plots indexes versus frequency for three particular sets of (l_{in}, l_b) values, where green points show the desired indexes satisfying $n_{\text{TE}} = n_{\text{TM}}$ at the operation frequency. In the same manner, we can obtain a series of indexes and the corresponding (l_{in}, l_b) values, which will be used to calculate the index functions versus geometric

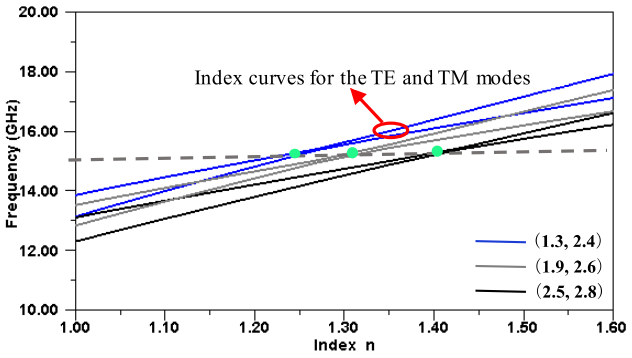

Fig. 8. Indexes versus frequency for three different sets of (l_{in}, l_b). For each set, the two curves show the index overlap of the TE and TM modes. The operation frequency of the HS is 15 GHz. Three green points indicate the desired indexes satisfying $n_{\mathrm{TE}} = n_{\mathrm{TM}}$ at the operation frequency.

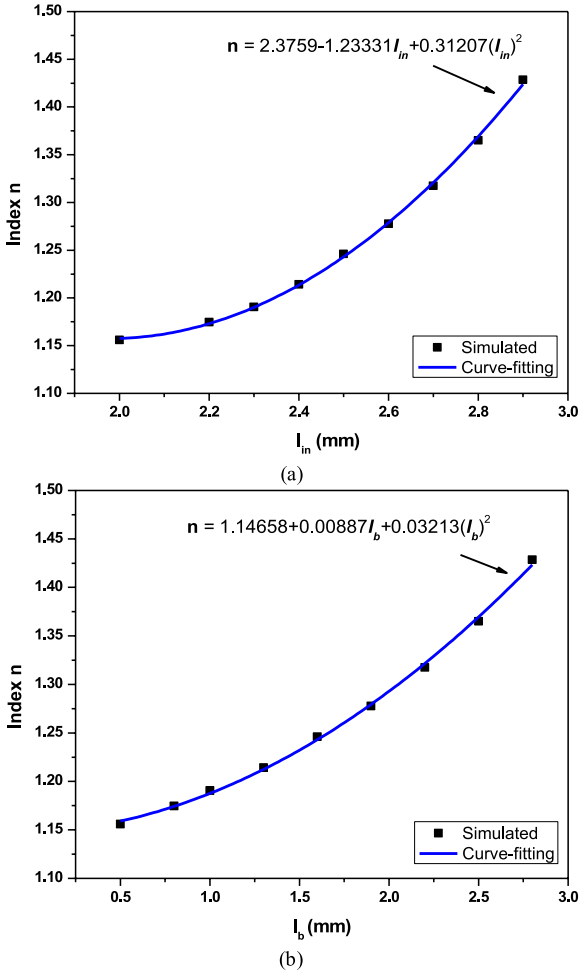

Fig. 9. Index versus lengths (a) l_{in} and (b) l_b of the loop-wire unit cell in square lattice.

parameters, as will be shown in Fig. 9. It is worth noting that, l_{in} and l_b have a dominant effect on the dispersion curves of the TE mode and TM mode, respectively, which is intuitive because the loop FSS dominantly supports the TE mode and wire-grid FSS dominantly supports the TM mode.

The index n, i.e., $n = n_{\mathrm{TE}} = n_{\mathrm{TM}}$, as a function of l_{in} and l_b at a frequency of 15 GHz is given

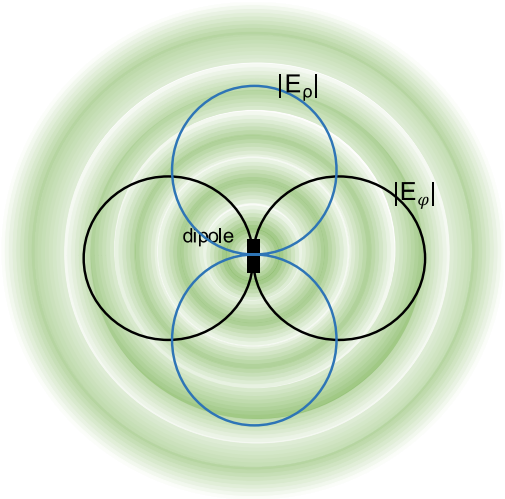

Fig. 10. Circumferential illumination of an HS by the x-directed electric dipole. The HS supports both TE and TM modes.

in Fig. 9(a) and (b), respectively. The scatter points are obtained from HFSS simulations by the same way as shown in Fig. 8, and the blue curves are obtained by nonlinear curve fit. For a given index, the values of l_{in} and l_b can be uniquely determined by solving these two fitting functions. Therefore, both layers are sinusoidally modulated for each HS constituted by this type of unit cells.

B. Holographic Surface Design

The field distributions on a polarization-insensitive HS excited by a small x-directed electric dipole are shown in Fig. 10. Because the HS can support both TE and TM modes, both E_ρ and E_φ can propagate on the surface. Assume the excitation of the x-directed dipole has the same expression as that in Section III, i.e., $E_0\vec{x}$. According to (8)

$$E_\rho = E_0 \cos(\varphi) \quad \text{and} \quad E_\varphi = -E_0 \sin(\varphi). \tag{14}$$

Fig. 10 shows the field distributions of E_ρ and E_φ on the HS structure. As a result, circularly symmetric E- and H-plane beamwidths can be achieved because the amplitude of the circumferential illumination of the dipole is constant.

A sinusoidally modulated HS constituted by loop-wire unit cells is designed by using function (13) with $X = 1.3$ and $M = 0.13$. A quarter of the HS in square lattice is shown in Fig. 11. Symmetric boundaries are used to simplify the simulation. As shown in Fig. 11, both the top layer (loops) and the bottom layer (grid-wires) are sinusoidally modulated. The HS works at a frequency of 15 GHz. The radius of the simulated HS is $R = 6\lambda_0$ (λ_0 is the free-space wavelength at 15 GHz.). To examine the electromagnetic properties of the proposed HS, a lumped port with polarization aligned with the x-axis is assigned at the center of the bottom layer of the HS structure.

The performance of the proposed HS is examined by HFSS simulations. Fig. 12 shows the radiation patterns of the proposed HS. As can be seen from Fig. 12, the E- and H-plane patterns are nearly the same, especially for the forward

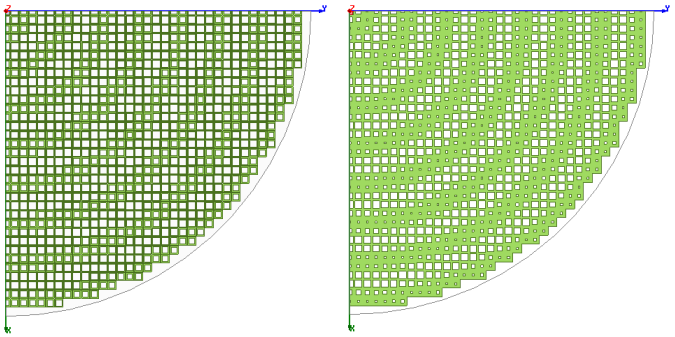

(a) (b)

Fig. 11. Quarter of the modulated HS composed of loop-wire unit cells in square lattice. (a) Top layer pattern. (b) Bottom layer pattern. Symmetric boundaries are used to simplify the simulation. X and M in (13) are 1.3 and 0.13, respectively.

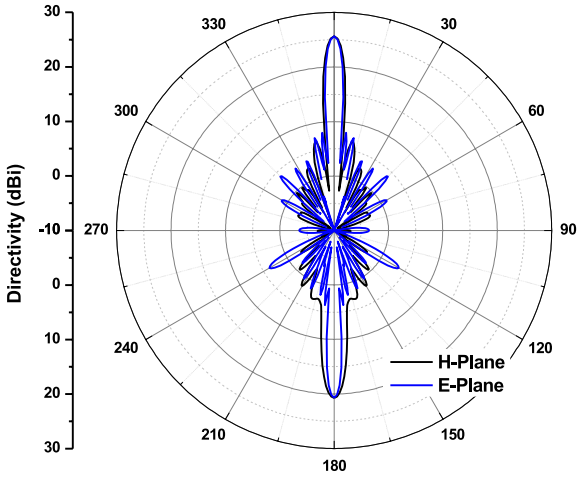

Fig. 12. Simulated radiation patterns with a maximum directivity of 25.6 dBi at $\theta = 0°$ direction and 20.7 dBi at $\theta = 180°$ direction. The return loss due to impedance mismatch is not included in the radiation patterns.

beam ($\theta = 0°$). However, for the backward beam ($\theta = 180°$), the beamwidth in the H-plane is noticeably wide compared to that in the E-plane. This is due to the lumped port excitation, which is directly attached to bottom layer, i.e., the wire-grid layer. As is mentioned before, the wire-grid layer would have a strong effect on the TM mode and therefore, for the backward beam, the beamwidth of the H-plane pattern is wider than that of the E-plane pattern. In the whole, such a pencil beam demonstrates that a rotationally symmetric E- and H-plane beamwidth can be achieved when the HS can support both TE and TM modes simultaneously. Therefore, a high aperture efficiency can be predicted. In fact, the aperture efficiency is 25.5% when considering the forward beam only and 33.7% when including both the forward and the backward beams, which demonstrates a great improvement compared with the aperture efficiency reported in Section III.

The field distributions of E_x and E_y components of an HS supporting both TE and TM modes can be derived as follows.

Since

$$\vec{e_\rho} = \vec{e_x}\cos(\varphi) + \vec{e_y}\sin(\varphi). \tag{15}$$

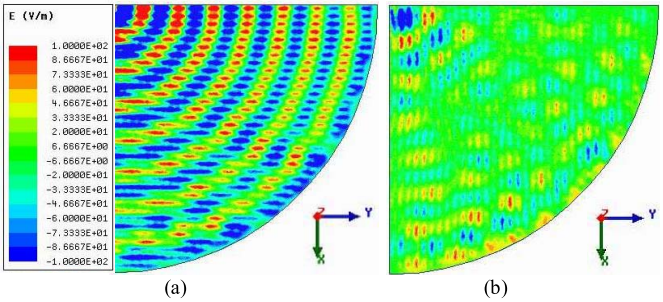

(a) (b)

Fig. 13. Field distributions of (a) E_x and (b) E_y components at a distance of 1 mm above the surface.

According to (10), (14), and (15), the E_x and E_y components on the HS structure have the following forms:

$$E_x = -E_\varphi \sin(\varphi) + E_\rho \cos(\varphi) = E_0 \tag{16}$$

$$E_y = E_\varphi cos(\varphi) + E_\rho \sin(\varphi) = 0. \tag{17}$$

Expressions (16) and (17) manifest that the E_x component remains constant at the HS surface with the same magnitude as the excitation and is independent of the azimuthal angle φ, while the E_y component is always zero.

Fig. 13 plots the field distributions of E_x and E_y components on a reference plane at a distance of 1 mm above the HS. As can be seen from Fig. 13(a), contrasting with those in Fig. 6(a), the E_x component is distributed along the whole surface, as is consistent with (16). Meanwhile, the E_y component is very weak over the whole surface, which agrees well with (17). Therefore, for the proposed polarization-insensitive HS, an x-directed dipole can fully illuminate the HS, which contributes to its high aperture efficiency.

Fabrication and measurements are carried out to verify the simulations. In simulation, the HS is excited by a lumped port. Similarly, in experiment, the HS is excited by an SMA probe with the inner conductor soldered to one edge of the wire-grid (bottom layer) and the outer conductor soldered to the other edge of the wire-grid along the x-axis. Fig. 14 shows the measured radiation patterns, which agree well with those in Fig. 12. The fabricated HS panel is also provided in Fig. 14. As can be seen from Fig. 14, the beamwidths in the E- and H-plane are nearly the same. Compared with simulation, a slightly higher side lobe level appears around θ from 90° to 120° due to the SMA probe feed on the bottom layer.

V. Polarization-Insensitive Holographic Surface Design Using Loop-Wire Cells in Hexagonal Lattice

A. Unit Cell Design

Square and hexagonal lattices are two commonly seen lattice types. The effects of these two lattice types on dispersion curves have been investigated by using the loop-wire configuration in [17], which demonstrates that surface waveguides with a hexagonal lattice exhibit better performance in the aspect of dispersion isotropy than those with a square lattice. In this section, an HS using hexagonal loop-wire unit cells, which can support both TE and TM modes propagation, is

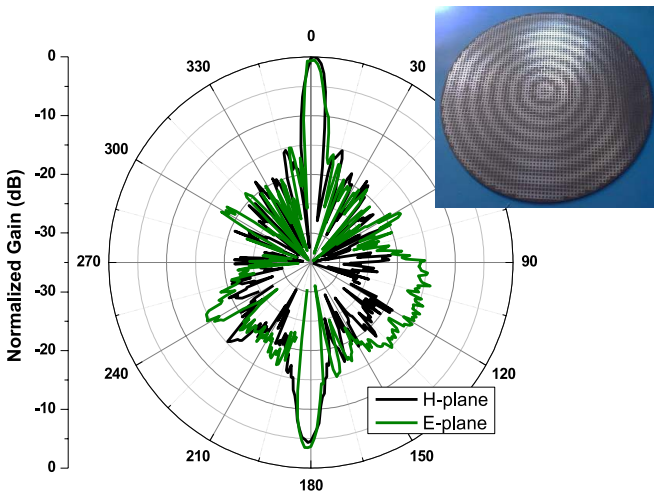

Fig. 14. Fabricated HS panel and its measured radiation patterns.

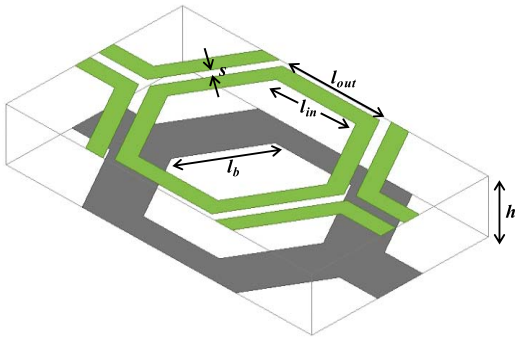

Fig. 15. Loop-wire unit supercell in hexagonal lattice.

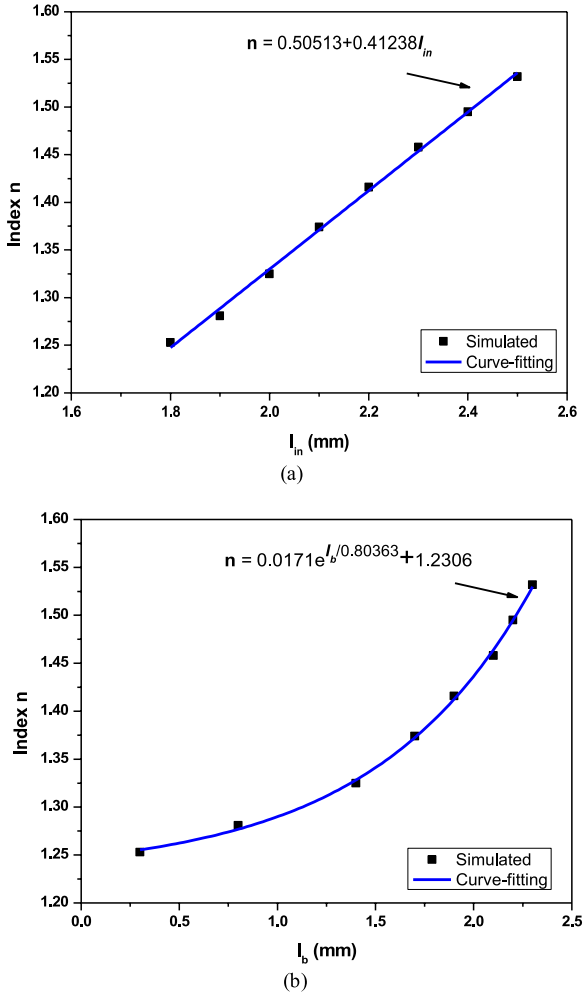

Fig. 16. Index versus lengths (a) l_{in} and (b) l_b of the loop-wire unit cell in hexagonal lattice at a frequency of 13.5 GHz.

proposed following the same design procedure as that in Section IV. For the sake of calculation, as shown in Fig. 15, a rectangular unit supercell instead of a hexagonal one is chosen for simulation. As shown in Fig. 15, a rectangular supercell consisted of hexagonal unit cells in terms of discrete loop-FSS for the top layer and continuous wire-FSS for the bottom layer is presented. A conductive hexagonal loop and a conductive wire-grid are printed at the top and bottom layer of a dielectric with a thickness of $h = 1.575$ mm and relative dielectric constant of $\varepsilon_r = 2.2$. The outer edge length of the square ring is kept as a constant of $l_{\text{out}} = 2.8$ mm. The lengths of the inner edges of the square loop and the wire-grid are l_{in} and l_b, respectively. The gap between two adjacent loops is $s = 0.25$ mm.

Next, the relationship between index and geometric parameters of the hexagonal loop-wire unit cell needs to be determined. The index of the TE mode and the TM mode can be tuned simultaneously (i.e., $n_{\text{TE}} = n_{\text{TM}}$) when lengths l_{in} and l_b are properly chosen. The index n ($n = n_{\text{TE}} = n_{\text{TM}}$) versus lengths l_{in} and l_b at a frequency of 13.5 GHz is given in Fig. 16(a) and (b), respectively, where the points are obtained from HFSS simulations and blue curves are obtained by curve fitting.

B. Holographic Surface Design

An HS in hexagonal lattice is designed using the hexagonal unit cells presented in Fig. 15 in this section. It is worth mentioning that the working principle of this HS is the same as that of the square lattice, which is analyzed in Section IV. Due to the loop-wire configuration, both of them are able to support both TE and TM modes at the operation frequency, and therefore pencil beams with circularly symmetric beamwidth in both the E- and H-plane can be obtained. In this section, the detailed analysis of the proposed HS is omitted for concision. The proposed HS, as shown in Fig. 17, is generated by using function (13) with $X = 1.41$ and $M = 0.13$. A lumped port at the bottom layer with polarization aligned with x-direction is used to illuminate the surface. The HS works at a frequency of 13.5 GHz. The radius of the simulated HS is $R = 5.59\lambda_0$ (λ_0 is the free-space wavelength at 13.5 GHz).

The simulated radiation performance is shown in Fig. 18. As can be seen in Fig. 18, a pencil beam is achieved both in the E- and H-plane. Especially for the forward beam ($\theta = 0°$), the beamwidths of the patterns in both planes are nearly the same. Due to the bottom-layer excitation, the beamwidth of the H-plane is slightly larger than that in the E-plane for

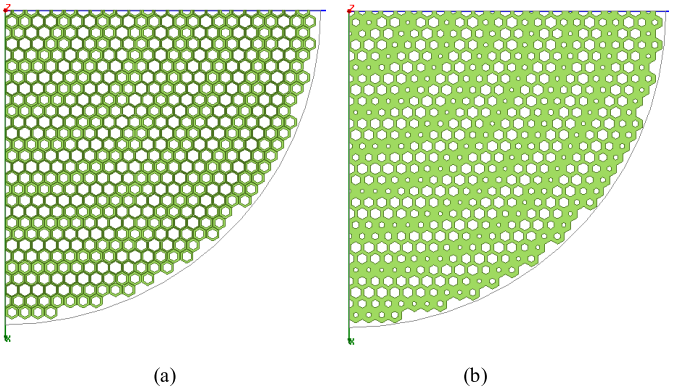

(a) (b)

Fig. 17. Quarter of the proposed HS with symmetric boundaries in hexagonal lattice. (a) Top layer pattern. (b) Bottom layer pattern. X and M in (13) are 1.41 and 0.13, respectively.

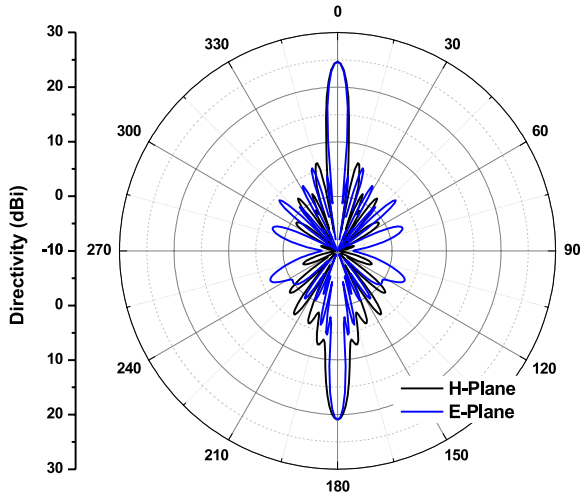

Fig. 18. Simulated radiation patterns with a maximum directivity of 24.7 dBi at $\theta = 0°$ direction and 20.9 dBi at $\theta = 180°$ direction. The return loss due to impedance mismatch is not included in the radiation patterns.

the backward beam ($\theta = 180°$). The same phenomenon can be found in Fig. 12. The corresponding aperture efficiency of the proposed HS is 23.8% when considering the forward beam only and 33.9% when considering both the forward beam and the backward beam. Almost the same aperture efficiencies are achieved for the HS in square lattice and that in hexagonal lattice. Therefore, both polarization-insensitive HS designs using loop-wire configuration in square and hexagonal lattice exhibit pencil beams and improved aperture efficiencies compared with a traditional scalar HS which has the drawback of polarization sensitivity.

Fig. 19 shows the fabricated panel of the proposed HS as well as the measured radiation patterns. As can be seen from Fig. 19, a narrow pencil beam is formed in the broadside direction. Compared with the simulated results, the beamwidth in the H-plane is slightly wider because of the errors resulting from the measurement setup and fabrication. Compared with simulations, a noticeably higher sidelobe appears in the lower hemisphere due to the SMA probe excitation, which is directly soldered to the center wire-grid cell on the bottom layer.

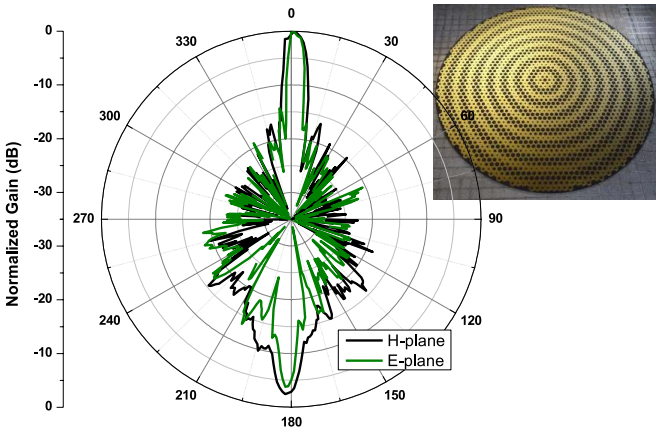

Fig. 19. Fabrication HS panel in hexagonal lattice and measured radiation patterns.

In the whole, the measurements agree well with the simulations.

VI. Conclusion

Traditional scalar HSs are able to support a TE or TM lower order Floquet mode, and have the drawback of polarization sensitivity, which results in a mismatch between the E- and H-plane beamwidths when excited by a horizontal dipole, and thus a low aperture efficiency. In this paper, loop-wire unit cells, which can support both TE and TM modes with the same phase velocity are utilized to design polarization-insensitive HSs. Instead of modulating the surface impedance to synthesize an HS, the refractive index is sinusoidally modulated in this paper, which provides convenience to the design of HSs for simultaneous TE and TM modes. Two HS designs using square and hexagonal loop-wire cells are proposed and experimentally studied to validate the characteristics of polarization insensitivity. Simulation and measurements show that pencil beams are achieved in the E- and H-plane of these two HS. This demonstrates that the proposed HS are insensitive to the polarization of coming waves and able to support both TE and TM modes. This kind of HS has the potential to be used in applications such as energy scavenging, because they can focus incoming waves to the center point of the antenna regardless of their polarization.

Acknowledgment

The authors would like to thank R. Quarfoth, the researcher at HRL Laboratories, and A. Li at UCSD for contributions during the work.

References

[1] B. H. Fong, J. S. Colburn, J. J. Ottusch, J. L. Visher, and D. F. Sievenpiper, "Scalar and tensor holographic artificial impedance surfaces," *IEEE Trans. Antennas Propag.*, vol. 58, no. 10, pp. 3212–3221, Oct. 2010.

[2] F. Caminita, M. Nannetti, and S. Maci, "Holographic surfaces realized by curvilinear strip gratings," in *Proc. 2nd Eur. Conf. Antennas Propag. (EuCAP)*, Nov. 2007, pp. 1–4.

[3] C. Rusch, J. Schäfer, H. Gulan, P. Pahl, and T. Zwick, "Holographic mmW-antennas with TE_0 and TM_0 surface wave launchers for frequency-scanning FMCW-radars," *IEEE Trans. Antennas Propag.*, vol. 63, no. 4, pp. 1603–1613, Apr. 2015.
[4] T. Su, Q. Zhang, R. Chen, and C. Sun, "Novel design of surface-wave holographic antenna miniaturization," *IEEE Antennas Wireless Propag. Lett.*, vol. 14, pp. 1077–1080, 2015.
[5] A. M. Patel and A. Grbic, "A printed leaky-wave antenna based on a sinusoidally-modulated reactance surface," *IEEE Trans. Antennas Propag.*, vol. 59, no. 6, pp. 2087–2096, Jun. 2011.
[6] S. K. Podilchak, L. Matekovits, A. P. Freundorfer, Y. M. M. Antar, and M. Orefice, "Controlled leaky-wave radiation from a planar configuration of width-modulated microstrip lines," *IEEE Trans. Antennas Propag.*, vol. 61, no. 10, pp. 4957–4972, Oct. 2013.
[7] A. A. Oliner and A. Hessel, "Guided waves on sinusoidally-modulated reactance surfaces," *IRE Trans. Antennas Propag.*, vol. 7, no. 5, pp. 201–208, Dec. 1959.
[8] G. Minatti, F. Caminita, M. Casaletti, and S. Maci, "Spiral leaky-wave antennas based on modulated surface impedance," *IEEE Trans. Antennas Propag.*, vol. 59, no. 12, pp. 4436–4444, Dec. 2011.
[9] M. Faenzi *et al.*, "Realization and measurement of broadside beam modulated metasurface antennas," *IEEE Antennas Wireless Propag. Lett.*, vol. 15, pp. 610–613, 2016.
[10] G. Minatti *et al.*, "Modulated metasurface antennas for space: Synthesis, analysis and realizations," *IEEE Trans. Antennas Propag.*, vol. 63, no. 4, pp. 1288–1300, Apr. 2015.
[11] A. T. Pereda *et al.*, "Dual circularly polarized broadside beam metasurface antenna," *IEEE Trans. Antennas Propag.*, vol. 64, no. 7, pp. 2944–2953, Jul. 2016.
[12] S. Pandi, C. A. Balanis, and C. R. Birtcher, "Design of scalar impedance holographic metasurfaces for antenna beam formation with desired polarization," *IEEE Trans. Antennas Propag.*, vol. 63, no. 7, pp. 3016–3024, Jul. 2015.
[13] X. Wan, Y. B. Li, B. G. Cai, and T. J. Cui, "Simultaneous controls of surface waves and propagating waves by metasurfaces," *Appl. Phys. Lett.*, vol. 105, no. 12, pp. 121603:1–121603:5, 2014.
[14] J. L. Gómez-Tornero, D. Blanco, E. Rajo-Iglesias, and N. Llombart, "Holographic surface leaky-wave lenses with circularly-polarized focused near-fields—Part I: Concept, design and analysis theory," *IEEE Trans. Antennas Propag.*, vol. 61, no. 7, pp. 3475–3485, Jul. 2013.
[15] Y. Liu, Y. Hao, K. Li, and S. Gong, "Wideband and polarization-independent radar cross section reduction using holographic metasurface," *IEEE Antennas Wireless Propag. Lett.*, vol. 15, pp. 1028–1031, Oct. 2015.
[16] A. Sutinjo, M. Okoniewski, and R. H. Johnston, "A holographic antenna approach for surface wave control in microstrip antenna applications," *IEEE Trans. Antennas Propag.*, vol. 58, no. 3, pp. 675–682, Mar. 2010.
[17] M. Li, S. Xiao, J. Long, and D. F. Sievenpiper, "Surface waveguides supporting both TM mode and TE mode with the same phase velocity," *IEEE Trans. Antennas Propag.*, vol. 64, no. 9, pp. 3811–3819, Sep. 2016.
[18] J. S. Colbum, D. F. Sievenpiper, B. H. Fong, J. J. Ottusch, J. L. Visher, and P. R. Herz, "Advances in artificial impedance surface conformal antennas," in *Proc. IEEE Antennas Propag. Soc. Int. Symp.*, Jun. 2007, pp. 3820–3823.

Mei Li (S'15-M'16) received the B.S. degree in electronic information science and technology from the Chengdu University of Information Technology, Chengdu, China, in 2010, and the Ph.D. degree in radio physics from the University of Electronic Science and Technology of China, Chengdu, in 2016.

From 2014 to 2016, she was with the Applied Electromagnetics Research Group, University of California at San Diego, San Diego, CA, USA, as a Visiting Graduate. Her current research interests include reconfigurable antennas, phased arrays, artificial electromagnetic structures, and holographic metasurfaces.

Shao-Qiu Xiao (M'05) received the Ph.D. degree in electromagnetic field and microwave engineering from the University of Electronic Science and Technology of China (UESTC), Chengdu, China, in 2003.

In 2004, he joined UESTC as an Assistant Professor. From 2004 to 2006, he was with the Wireless Communications Laboratory, National Institute of Information and Communications Technology, Tokyo, Japan, as a Researcher focusing on the planar antenna and smart antenna design and optimization. From 2006 to 2010, he was with UESTC as an Associate Professor, and is currently a Professor. He has authored or co-authored more than 160 technical journals, conference papers, books, and book chapters. His current research interests include planar antenna and phased array, microwave passive circuits, and time reversal electromagnetics.

Daniel F. Sievenpiper (M'94–SM'04–F'09) received the B.S. and Ph.D. degrees in electrical engineering from the University of California at Los Angeles, Los Angeles, CA, USA, in 1994 and 1999, respectively.

He was the Director of the Applied Electromagnetics Laboratory at HRL Laboratories, Malibu, CA, USA. He is currently a Professor with the University of California at San Diego, San Diego, CA, USA. He holds more than 70 issued patents and has authored 80 technical publications. His research interests included artificial impedance surfaces, conformal antennas, tunable and wearable antennas, and beam steering methods. His current research interests include antennas and electromagnetic structures.

Dr. Sievenpiper was a recipient of the URSI Issac Koga Gold Medal, in 2008. Since 2010, he has been an Associate Editor of the *IEEE Antennas and Wireless Propagation Letters*.